A comprehensive photometric study of the eclipsing SU UMa-type cataclysmic variable OY Carinae

Zhong-Tao Han[1], Sheng-Bang Qian[2], Fernández Lajús Eduardo[3,4], Wei-Wei Na[1], Hu-Shang Xu[1], Soonthornthum Boonrucksar[5], Ai-Jun Dong[6] and Ting-Ting Yang[1]

ABSTRACT

We present the photometric study of the eclipsing dwarf nova OY Car based on the ground-based observations and the archival data from TESS and AAVSO. Eclipse timing analysis shows a secular increase in the orbital period at a rate of $+5.70 \times 10^{-13} s\, s^{-1}$, and a cyclic period variation with an amplitude of 57.11 s and a period of 33.41 yrs. This period increase cannot be attributed to either the mass transfer or a period bouncer, suggesting the presence of an unrecognized mechanism. The cyclic oscillation is most effectively interpreted as a gravitational perturbation from an undetected circumbinary object. The potential tertiary companion should be a giant planet with a mass of $11.52 M_{Jup}$ in a circular orbit. TESS light curve contains one superoutburst and a normal outburst. Analysis of the eclipse depth versus the out-of-eclipse flux reveals a linear correlation during quiescence, with a lower slope before the superoutburst consistent with disk structure changes predicted by the thermal-tidal instability (TTI) model. Deviations from linearity during outbursts manifest as hysteresis loops, indicative of disk expansion and complex evolution. Eclipse analysis reveals that the normal outburst is of the outside-in type with varying hot spot contributions, while the superoutburst exhibits a 2.84-day $O - C$ modulation indicating a precessing

---

[1]Faculty of Mathematics and Physics, Yuxi Normal University, Phoenix Road 134, 653100 Yuxi, China; hzt@yxnu.edu.cn

[2]Department of Astronomy, School of Physics and Astronomy, Key Laboratory of Astroparticle Physics of Yunnan Province, Yunnan University, Kunming 650091, Peoples Republic of China;

[3]Facultad de Ciencias Astronómicas y Geofísicas, Universidad Nacional de La Plata, Paseo del Bosque s/n, 1900 La Plata, Buenos Aires, Argentina;

[4]Instituto de Astrofísica de La Plata (CCT La PlataCONICET/UNLP), 1900 La Plata, Argentina;

[5]National Astronomical Research Institute of Thailand, Ministry of Higher Education Science Research and Innovation, 260 Moo 4, T. Donkaew, A. Maerim, Chiangmai, 50180, Thailand;

[6]Guizhou Provincial Key Laboratory of Radio Data Processing, School of Physics and Electronic Sciences, Guizhou Normal University, Guiyang 550001, People's Republic of China.

eccentric disk. Positive superhumps are detected with a period of 0.064556 d, yielding a mass ratio $q = 0.1049$. We also study the superhump evolution in OY Car, which shows a standard three-stage evolution with a positive period derivative in stage B, reflecting disk evolution and resonance effects.

Subject headings: Close binary stars (254); Eclipsing binary stars (444); Cataclysmic variable stars (203); Dwarf novae (418)

1. Introduction

Accreting white dwarfs are commonly observed within close binary systems, featuring orbital periods spanning from a few minutes to several hours. The white dwarf star accretes material from a companion star, which can be either a main sequence star or another white dwarf. Through the accretion process, the material from the companion star forms an accretion disk around the white dwarf, leading to a variety of astrophysical phenomena such as novae, dwarf novae and AM CVn stars. As a type of accreting white dwarf binaries, the dwarf novae often show multiple optical outbursts spanning magnitudes of 2 to 8, with recurrence times ranging from days to decades (see Warner 2003). The outburst mechanism is likely the release of gravitational energy due to a thermal-viscous instability in the accretion disk, associated with the partial ionization of hydrogen (see Osaki 1996; Lasota 2001). Additionally, some dwarf novae exhibit outbursts with durations spanning approximately two weeks to a month, which are slightly brighter than normal outbursts and are referred to as superoutbursts. Such phenomena is attributed to a combination between the thermal instability and tidal interaction of the disc with the donor star (Osaki 1989). More specifically, the former trigger a normal dwarf nova outburst, resulting in the expansion in the disc radius up to a critical value (i.e., 3:1 resonance radius) where the disc became tidally unstable and a superoutburst occurred. The most prominent feature of superoutburst is the presence of superhumps, which are periodic brightness modulations with periods several percent longer or shorter than the orbital period of the system, corresponding to positive and negative superhumps, respectively (e.g., Vogt 1974, 1982; Motch 1981; Wood et al. 2011). The origin of positive superhumps is the precession of an elliptical and asymmetric disc produced by the tidal torques from the secondary star (Whitehurst 1988; Whitehurst & King 1991), and the negative superhumps are believed to result from the precession of the tilted accretion disk (e.g., Bonnet-Bidaud et al. 1985; Patterson 1999; Harvey et al. 1995; Wood et al. 2009; Montgomery 2009; Kimura & Osaki 2021).

The superoutburst is one of most important hallmarks to identify the SU UMa-type dwarf novae. OY Carinae (hereafter OY Car) is an eclipsing SU UMa-type star with a short binary period of 1.51 hr and has been extensively studied in the last few decades at wavelengths ranging from optical to X-rays (e.g., Copperwheat et al. 2012; Woudt et al. 2009; Mauche et al. 1998, 2000; Billington et al. 1996; Pandel et al. 2005; Baskill et al. 2005; Ramsay et al. 2001a,b). Its superoutbursts have been observed photometrically by Krzeminski & Vogt (1985), Schoembs (1986), Bruch et al. (1996) and Pratt et al. (1999). The properties of the superhumps in OY Car have also been studied in the following years (e.g., Smak 2013; Kato et al. 2017 and references therein). However, early ground-based observations suffer from a few drawbacks to probing the outburst properties and light curve morphology as well as to investigating the superhump evolution due to the randomized gaps and the limited length of nightly light curves. The continuous monitoring by the Transiting Exoplanet Survey Satellite (TESS) (Ricker et al. 2014) has allowed these problems to be overcome, enabling a test of the theory of dwarf-nova outbursts.

Another distinct feature in the light curves of OY Car is the deep eclipses due to the high orbital inclination ($\sim 83°$, Wood et al. 1989; McAllister et al. 2019). This property can constrain the binary parameters well and reveal orbital period variations, which provide an opportunity to test the evolutionary theory of cataclysmic variables (CVs) and to pick up circumbinary companions. Moreover, the eclipse proves to be a valuable tool for the investigation of accretion disks. For example, Horne (1985) proposed the eclipse mapping method to address the problem of the disk evolution with time during outburst (Baptista 2016 for a detailed overview). As a result based on the above characteristics, OY Car is an interesting object which can be used to explore the nature of accreting white dwarfs in CVs.

In this paper we report the ground-based and TESS photometry of OY Car, and then we present a detailed analysis of the optical variability of this system including eclipse timings, normal outbursts and superoutbursts. We describe the observations in Section 2. We perform a study of the orbital period variations and an analysis of TESS photometry of OY Car in Section 3. We discuss the physical causes of the eclipse timing variations and the outburst properties in Section 4. The results are summarized in Section 5.

2. Data

2.1. Ground-based Photometry

OY Car was monitored photometrically from November 2008 to February 2025 with the 2.15 m Jorge Sahade telescope at the Complejo Astronomico El Leoncito (CASLEO), San Juan, Argentina. This telescope equipped with a Versarray 2048B CCD camera manufactured by the Roper Scientific, Princeton Instruments. The field view of the telescope is $5.1' \times 5.1'$. No filter was used during the observations in order to improve the time resolution. The star was observed for $\sim 20 - 120$ min each night with a 4-5 s exposure time bring about a cadence of ~ 9 s. The standard reduction of the data was performed using the aperture photometry package of IRAF (the Image Reduction and Analysis Facility) software (see Tody 1986, 1993). Processing consists of the basic processing steps by subtracting bias, dark and correcting flat-field. We used the differential photometry method to extract the light curves. The comparison star is the same for all observations and has been checked to be a no-variable star. Eight eclipse profiles during quiescence are shown in Figure 1. These eclipse shape exhibits a two-step characteristic, which implies that the ingress and egress times of white dwarf can be distinguish clearly. This system is thus clean mid-eclipse timing source, and enables us to measure eclipse times precisely. We apply the derivative method proposed by Wood et al. (1985) to determine the mid-eclipse times of OY Car. The detailed process can be seen in Han et al. (2017, 2023). The results are listed in Table 1.

2.2. AAVSO Data

We inspected the light curves of OY Car retrieved from the American Association of Variable Star Observers (AAVSO) International Database[1] and obtained a long photometric time-series data. Figure 2 plots the long-term AAVSO light curves in Vis/V band, spanning a total of 60.4 yrs between 1963 June 26 and 2023 November 13. Note that the unreliable observations in Vis have been excluded. The light curves are characterised by two main types of variability: outbursts and eclipses, and the former can also be divided into the superoutbursts and normal outbursts. The quiescent magnitude is very difficult to accurately measure due to the variations in the out-of-eclipse brightness and the eclipses. We rough estimate a quiescent level of ~ 15.4 mag. In addition, the light curve in V-band during quiescence contains many eclipses, which can be used for eclipse timings. The bottom panel of Figure 2 shows an enlarged view of the segment enclosed by the red rectangle. Using the same method above, 17 mid-eclipse times are obtained and also listed in Table 1. Likewise, these mid-eclipse times are also converted to barycentric Julian dates in barycentric dynamical time (BJD_TDB).

---

[1]https://www.aavso.org/LCGv2/

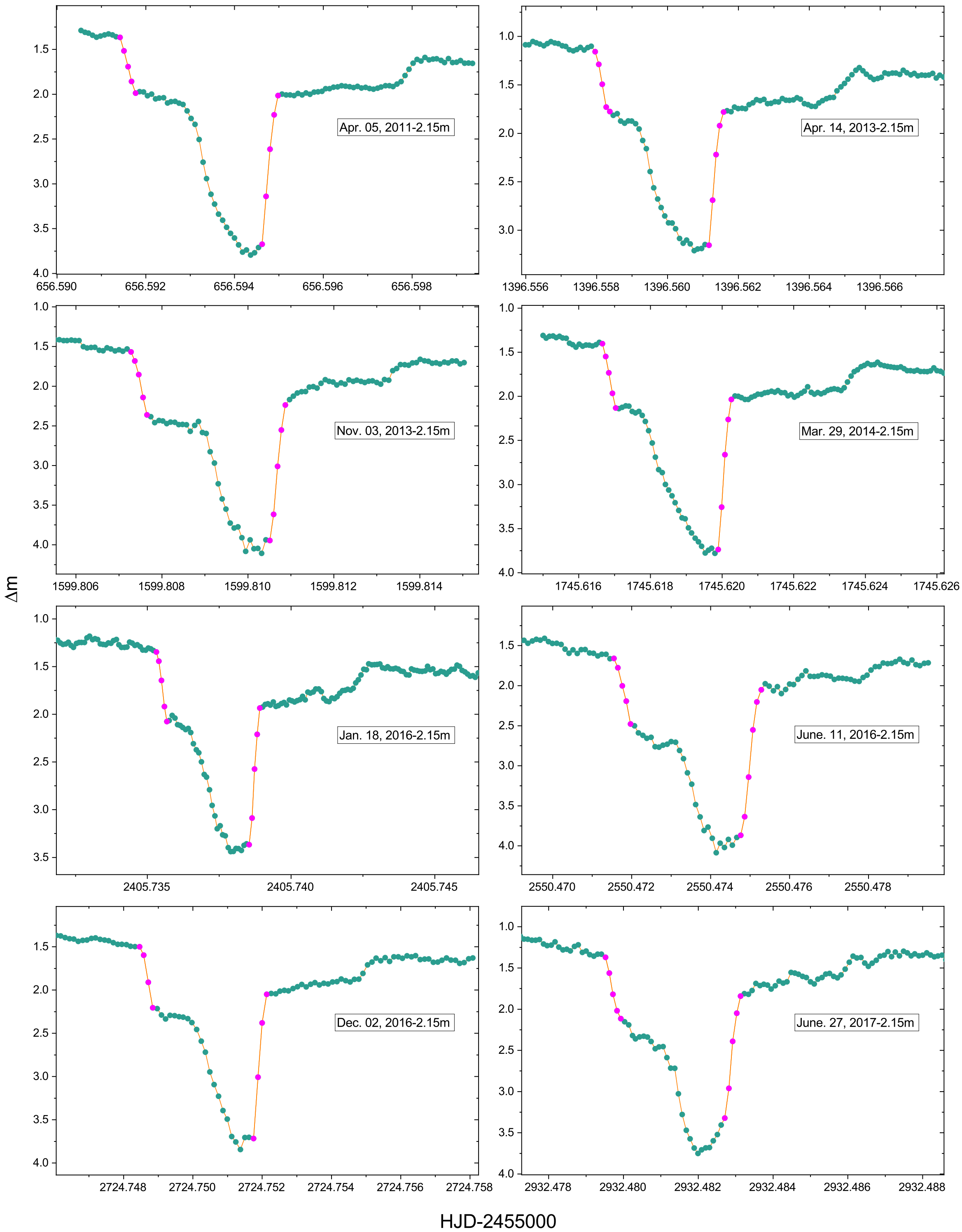

Fig. 1.— Eight sample eclipse light curves of OY Car during quiescence in the N band observed with 2.15 m Jorge Sahade telescope in Argentina. The eclipse light curves displays the properties of the white dwarf and bright spot eclipses. The magenta refers to the ingress and egress of the white dwarf.

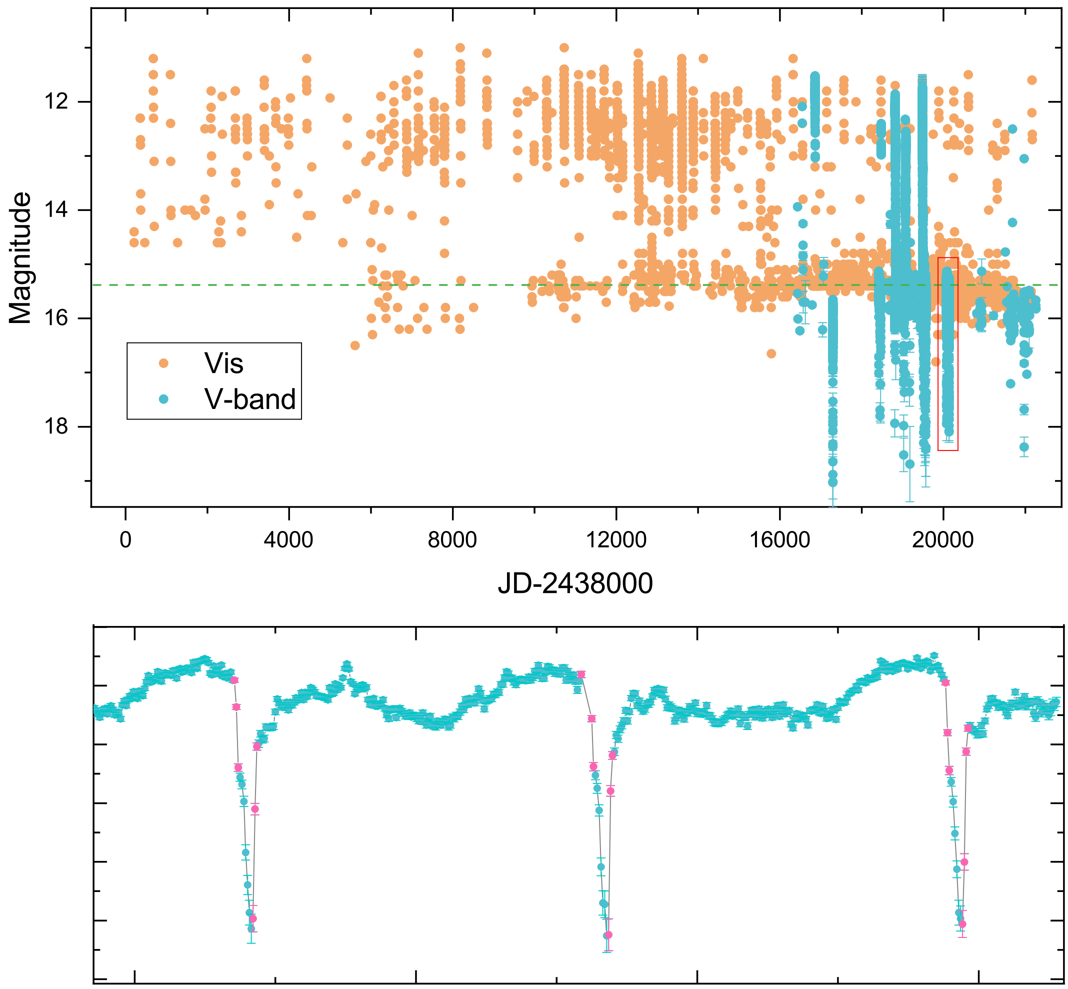

Fig. 2.— Archival AAVSO light curve of OY Car during 1963 June 26 to 2023 November 13. The navy blue solid circles represent the V-band data, the orange solid circles correspond to the visual observations. The light curve in the lower panel is a zoom to a part of the V-band data, displaying clear white dwarf eclipses.

2.3. TESS Observations

The main goal of the Transiting Exoplanet Survey Satellite (TESS) is to detect small transiting planets that orbit bright stars (Ricker et al. 2015, 2016; Collins et al. 2018). TESS observes in sectors, in which each sector, totalling 27.4 days, is separated into two continuous observation orbits of ∼13.7 days and interrupted briefly to download the data. Generally, the duration of dwarf nova oubursts is $\sim 2-20$ days. Therefore, TESS data allow us to explore the properties of outbursts and oscillations with time in CVs (e.g. Court et al. 2019; Han et al. 2021). TESS observed OY Car during Cycle 1 (26 March 2019-20 May 2019), during Cycle 3 (02 April 2019-26 May 2021) and during Cycle 5 (06 April 2023-01 June 2023) at 2 min cadence. The light curves were downloaded from the Mikulski Archive for Space Telescopes web service[2]. Note that we have considered only the data with the quality flag value of 0 in this work. Figure 3 displays the observed TESS Cycle 1 and 3 (Sectors 11 and 37) light curves of OY Car, showing a superoutburst lasting ~ 18 days and a normal outburst lasting ~ 4 days. The detrended light curve by subtracting the outburst shape is also plotted in Figure 3. We can clearly see that the eclipse depth undergoes significant change over the outburst cycle, and the superhumps appeared at the superoutburst peak. The nature of outbursts and eclipses will be studied and discussed in the following sections.

3. Data Analysis and Results

3.1. Improved Orbital Ephemeris

Several studies have been published to investigate the orbital period changes of OY Car (e.g., Vogt et al. 1981; Cook 1985; Wood et al. 1989; Greenhill et al. 2006; Han et al. 2015 and Pilarčík et al. 2018). In several studies before 2006, the orbital period of OY Car showed no obvious changes. In 2006, Greenhill et al. found that the orbital period of OY Car has a possible sinusoidal variation in the $O-C$ diagram. Han et al. (2015) performed period change study of OY Car and confirmed that its orbital period may indeed have a periodic oscillation. Pilarčík et al. (2018) further updated the $O-C$ curve and improved the sinusoidal ephemeris. Combine new eclipse times in Table 1 with published data in literature, we constructed the latest $O-C$ diagram by using the ephemeris from Wood et al. (1989)

$$Min.(BJD) = 2443993.553813(9) + 0.0631209239(5) \times E. \tag{1}$$

[2]https://mast.stsci.edu/portal/Mashup/Clients/Mast/Portal.html

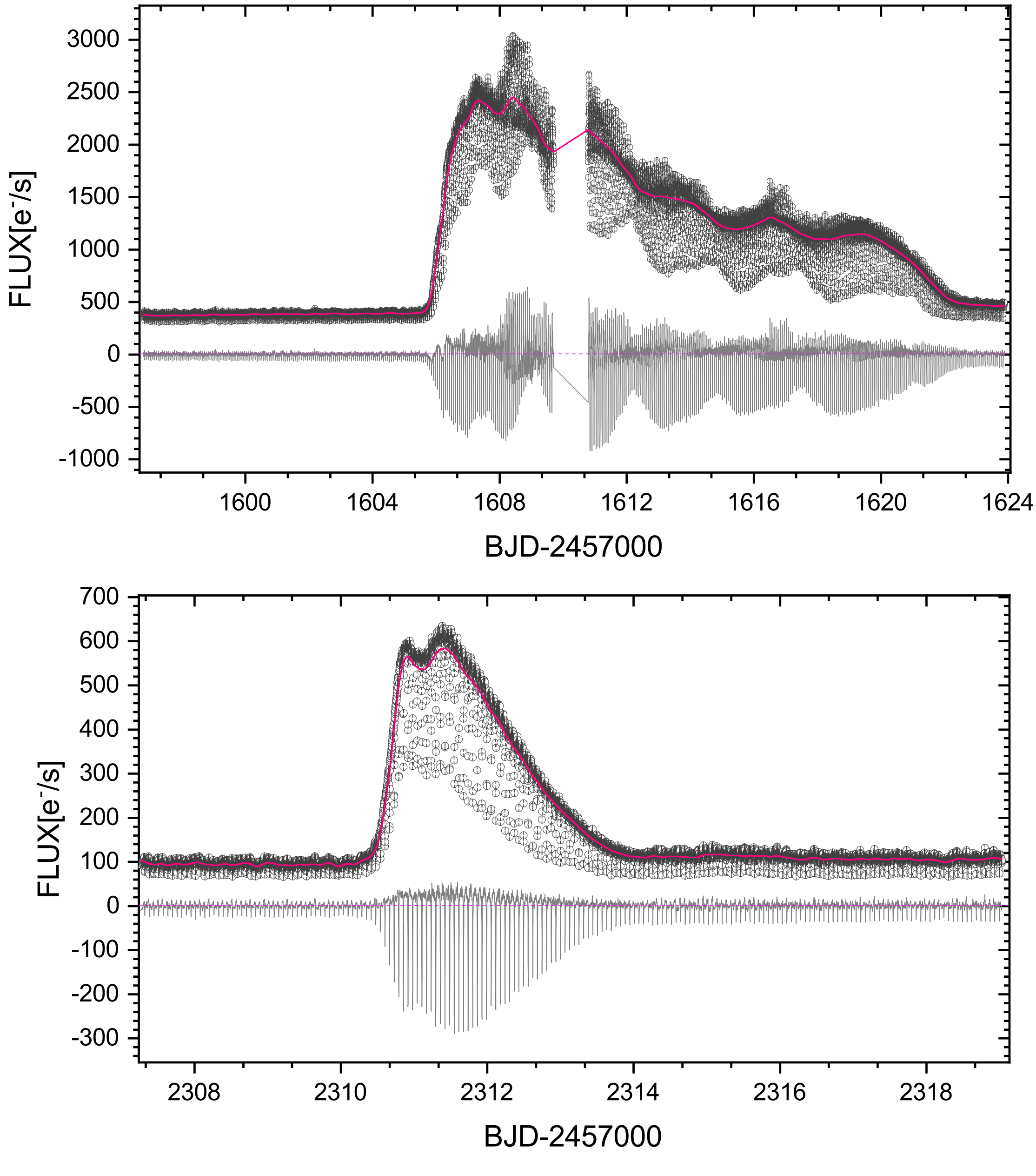

Fig. 3.— TESS light curve of OY Car, displaying a superoutburst in the top panel and a normal outburst in the bottom panel, as well as clear eclipse features. The red solid line represents the smoothed light curve using the LOESS fit. The gray line is the detrended light curve by subtracting the smoothed light curve.

Table 1: New mid-eclipse times of OY Car.

Date	Min.(HJD)	Min.(BJD)	Epoch	O-C	Err	Telescopes	Filters
2008 Nov 28	2454798.84312	2454798.84387	171184	-0.00218	0.00005	2.15 m	N
2009 Jan 14	2454845.67889	2454845.67965	171926	-0.00213	0.00005	2.15 m	N
2010 Apr 08	2455295.09965	2455295.10042	179046	-0.00233	0.00010	AAVSO	V
2010 Apr 08	2455295.16285	2455295.16362	179047	-0.00226	0.00010	AAVSO	V
2010 Apr 08	2455295.22595	2455295.22672	179048	-0.00228	0.00010	AAVSO	V
2010 Dec 06	2455536.85361	2455536.85438	182876	-0.00152	0.00020	2.15 m	N
2010 Dec 07	2455537.80018	2455537.80096	182891	-0.00175	0.00020	2.15 m	N
2011 Apr 03	2455654.57336	2455654.57413	184741	-0.00229	0.00005	2.15 m	N
2011 Apr 05	2455656.59318	2455656.59395	184773	-0.00233	0.00005	2.15 m	N
2012 Apr 15	2456033.48817	2456033.48894	190744	-0.00238	0.00005	2.15 m	N
2013 Apr 13	2456395.67604	2456395.67682	196482	-0.00237	0.00005	2.15 m	N
2013 Apr 14	2456396.55972	2456396.56050	196496	-0.00238	0.00005	2.15 m	N
2013 Nov 03	2456599.80910	2456599.80988	199716	-0.00237	0.00005	2.15 m	N
2013 Nov 05	2456601.82896	2456601.82974	199748	-0.00238	0.00005	2.15 m	N
2014 Mar 29	2456745.61846	2456745.61924	202026	-0.00235	0.00005	2.15 m	N
2014 Mar 30	2456746.69148	2456746.69226	202043	-0.00238	0.00005	2.15 m	N
2014 Mar 31	2456747.63831	2456747.63909	202058	-0.00237	0.00005	2.15 m	N
2015 Jan 03	2457026.19087	2457026.19165	206471	-0.00244	0.00010	AAVSO	V
2016 Jan 16	2457403.84351	2457403.84429	212454	-0.00229	0.00005	2.15 m	N
2016 Jan 18	2457405.73711	2457405.73789	212484	-0.00232	0.00005	2.15 m	N
2016 Jan 19	2457406.62083	2457406.62161	212498	-0.00229	0.00005	2.15 m	N
2016 Jun 10	2457549.52665	2457549.52743	214762	-0.00225	0.00005	2.15 m	N
2016 Jun 11	2457550.47339	2457550.47417	214777	-0.00232	0.00005	2.15 m	N
2016 Jun 12	2457551.54648	2457551.54726	214794	-0.00229	0.00005	2.15 m	N
2016 Oct 11	2457672.86490	2457672.86568	216716	-0.00227	0.00005	2.15 m	N
2016 Dec 02	2457724.75033	2457724.75110	217538	-0.00225	0.00005	2.15 m	N
2017 Jun 27	2457932.48127	2457932.48206	220829	-0.00226	0.00005	2.15 m	N
2017 Nov 16	2458074.18781	2458074.18860	223074	-0.00219	0.00010	AAVSO	V
2017 Nov 16	2458074.25093	2458074.25172	223075	-0.00219	0.00010	AAVSO	V
2017 Nov 24	2458082.14109	2458082.14189	223200	-0.00214	0.00010	AAVSO	V
2017 Nov 24	2458082.20416	2458082.20495	223201	-0.00219	0.00010	AAVSO	V
2017 Nov 25	2458083.15104	2458083.15183	223216	-0.00213	0.00010	AAVSO	V
2017 Nov 25	2458083.21399	2458083.21479	223217	-0.00230	0.00010	AAVSO	V
2018 Jan 18	2458137.11940	2458137.12019	224071	-0.00216	0.00010	AAVSO	V
2018 Jan 18	2458137.18251	2458137.18330	224072	-0.00217	0.00010	AAVSO	V
2018 Jan 18	2458137.24566	2458137.24645	224073	-0.00214	0.00010	AAVSO	V
2018 Jan 19	2458138.12935	2458138.13014	224087	-0.00214	0.00010	AAVSO	V
2018 Jan 19	2458138.19248	2458138.19327	224088	-0.00213	0.00010	AAVSO	V
2018 Jan 19	2458138.25558	2458138.25637	224089	-0.00216	0.00010	AAVSO	V
2019 Jun 06	2458640.50884	2458640.50964	232046	-0.00209	0.00005	2.15 m	N
2023 Jan 25	2459970.21465	2459970.21547	253112	-0.00164	0.00010	AAVSO	V
2023 May 25	2460089.51337	2460089.51419	255002	-0.00146	0.00005	2.15 m	N
2025 Feb 23	2460729.81213	2460729.81294	265146	-0.00136	0.00005	2.15 m	N

Figure 4 shows the updated $O-C$ curve, which has an approximately 46 years observational baseline. We have tried several solutions to fit these data, including the linear or/and quadratic plus sinusoidal model, and the linear or/and quadratic plus light travel time effect (LTTE) model. The results show that a quadratic plus sinusoidal ephemeris is the best solution, which can be represented by the following equation

$$O - C = \Delta T_0 + \Delta P_0 \times E + \beta E^2 + K \sin(2\pi/P_3 + \varphi). \quad (2)$$

Table 2 provides a summary of the fitting parameters and errors acquired by using the Levenberg−Marquardt method (Press et al. 1992). The weights are the inverse of the squared data point error. The fitted curve is also plotted in Figure 4. A small residual sum of squares ($\chi^2 = 9.77 \times 10^{-7}$) indicates that this is a good fit, although there is some deviations in the range of 50000 to 150000 cycles. We will discuss the possible reasons for the departure in Section 4.1. The result shows that the orbital period of OY Car, in addition to the long-term increase, also has a cyclic oscillation with an amplitude of 57.11(±0.86) s and a period of 33.41(±0.06) yrs. In Figure 4, the best-fitting ephemeris is indicated by the orange solid line in the top panel. The residuals from such a best-fitting model are plotted in the bottom panel.

Table 2: Orbital parameters of the circumbinary giant planet in OY Car.

Parameters	Quadratic *plus* sinusoidal model	Unit
Revised epoch, ΔT_0	$+7.76(\pm0.63) \times 10^{-4}$	days
Revised orbital period, ΔP_0	$-2.03(\pm0.16) \times 10^{-8}$	days
Rate of the linear period increase, β	$+3.60(\pm0.65) \times 10^{-14}$	days/cycle
The semi-amplitude, K	$6.61(\pm0.10) \times 10^{-4}$	days
Orbital period of the third body, P_3	33.41(±0.06)	years
Orbital phase of the third body, φ	73.34(±3.95)	deg
Projected semi-major axis, $a_{12} \sin i'$	0.114(±0.002)	au
Mass function, $f(m)$	$1.35(\pm0.06) \times 10^{-6}$	$M_\odot$
Mass of the third body, $M_3 \sin i'$	0.011(±0.003)	$M_\odot$
Orbital radius of the third body, d_3 ($i' = 90°$)	12.13(±0.36)	au
Residual sum of squares, χ^2	9.77×10^{-7}	–
Adjust R-squared, R^2	0.95	–

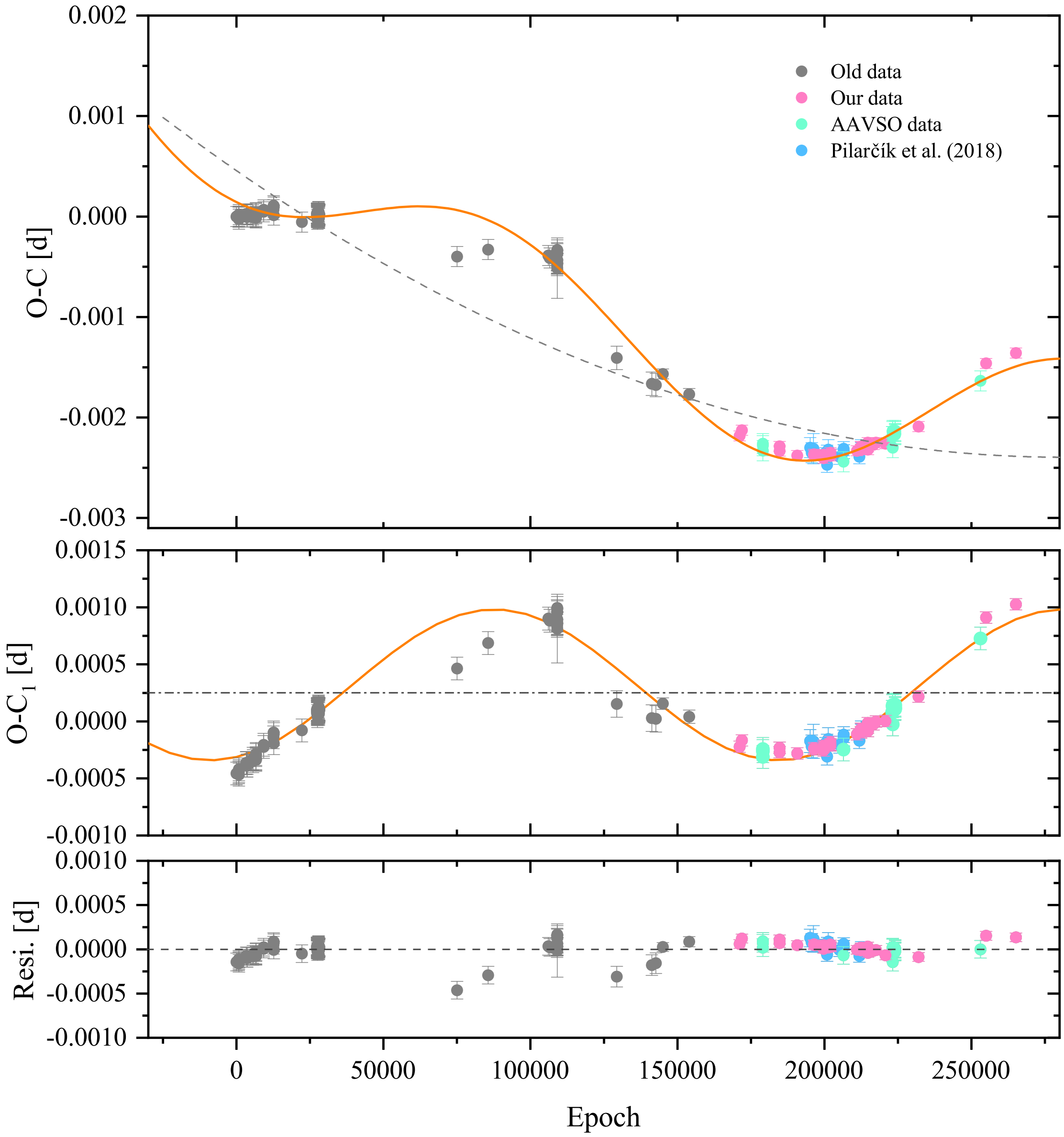

Fig. 4.— Updated $O-C$ diagram of OY Car constructed with a quadratic plus the sinusoidal ephemeris. The grey and light cyan points denote the historical timings, while the hot pink points refer to our eclipse timings and the mint green points denote the AAVSO data. The orange solid line and grey dashed line in the top panel represent the best-fit model and the quadratic term of the model, respectively. The middle panel shows the LTTE orbit and the bottom panel displays the fit residuals from the full ephemeris.

3.2. TESS Photometry Analysis

3.2.1. Eclipse Analysis during Outbursts

TESS light curves of OY Car are extremely diverse and complex, including outbursts, superhumps, oscillations and eclipses. Figure 3 shows a superoutburst starting on BJD 2458605 and a normal outburst starting on BJD 2459310. There is a significant change in depth and shape during the outburst cycle. To measure the depth, width, and time of the minimum light of the eclipses, we performed Gaussian fits on all eclipse curves and visually checked whether each fit was reasonable. The width was approximated by calculating the full width at half minimum (FWHM) for each fit through numerical methods. This method allowed us to identify any outliers or erroneous data points, ensuring the reliability of our results. We define the eclipse depth as the difference between the average out-of-eclipse flux and the minimum flux of the eclipses. This method is effective and well used for quiescent data and normal outbursts, but there is a significant uncertainty when the superhump appears. We also performed an $O - C$ analysis for all time of the minimum to study the eclipse variations during outburst and superoutburst. The $O - C$ values are calculated by using a new initial epoch, BJD 2458596.83097 for the superoutburst and BJD 2459307.32021 for the normal outburst. These parameters are plotted in Figure 5 and 6. We discuss these variations in Section 4.2.

To study how the periodic signals varied as a function of time, we constructed two weighted wavelet Z-transform (WWZ) power spectra from the detrended TESS light curves by using the VARTOOLS program (Hartman & Bakos 2016), as shown in the second panel of Figure 5 and 6. A frequency step of 0.1/T is used to calculate the WWZ transform up to a maximum frequency of 100 d^{-1}, where T is the time base-line of the light curve. In our analysis, we employ a time-shift step of 0.1 days to account for time-shifts spanning from the first to the last observation. In Figure 5, the power was concentrated around the orbital period and its second harmonic. The second harmonic signal is stronger than the orbital period during quiescence. At the outset of outburst, the second harmonic quickly disappeared and the orbital period returned to dominate, implying that this harmonic originates from the interaction of eclipses and orbital humps. The power begins to oscillate and the power spectrum shows distinct higher harmonics after the superhump appeared. Moreover, there is a quasi-periodic signal with a frequency of $\sim 3.49\ d^{-1}$ from BJD 2458599.44 to BJD 2458601.77. We suggest that the variable in mass transfer rate could be the cause of this signal. In Figure 6, the power was strongest at the orbital period and its second harmonic throughout the full light curve. This harmonic rapidly weakened during normal outburst, indicating that the orbital humps in outburst become weaker and disappear at maximum.

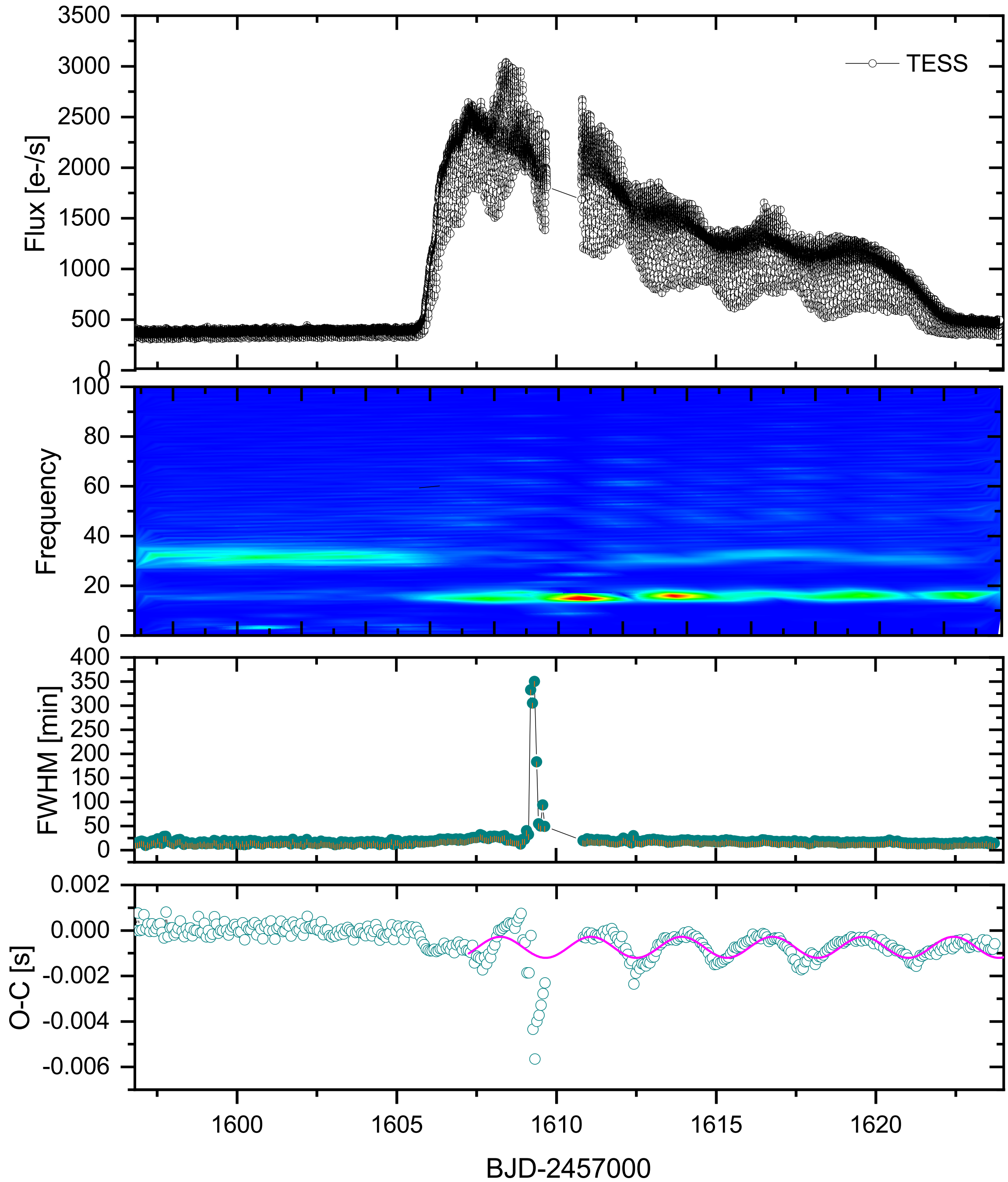

Fig. 5.— Top panel: the full TESS light curve of OY Car during superoutburst. From top to bottom, the remaining three panels show the weighted wavelet Z-transform around the orbital period's fundamental harmonic, the eclipse full width at half minimum, and the eclipse $O-C$ curve. The magenta line in the bottom panel represents the best-fitting sinusoid to the eclipse $O-C$ during superoutburst.

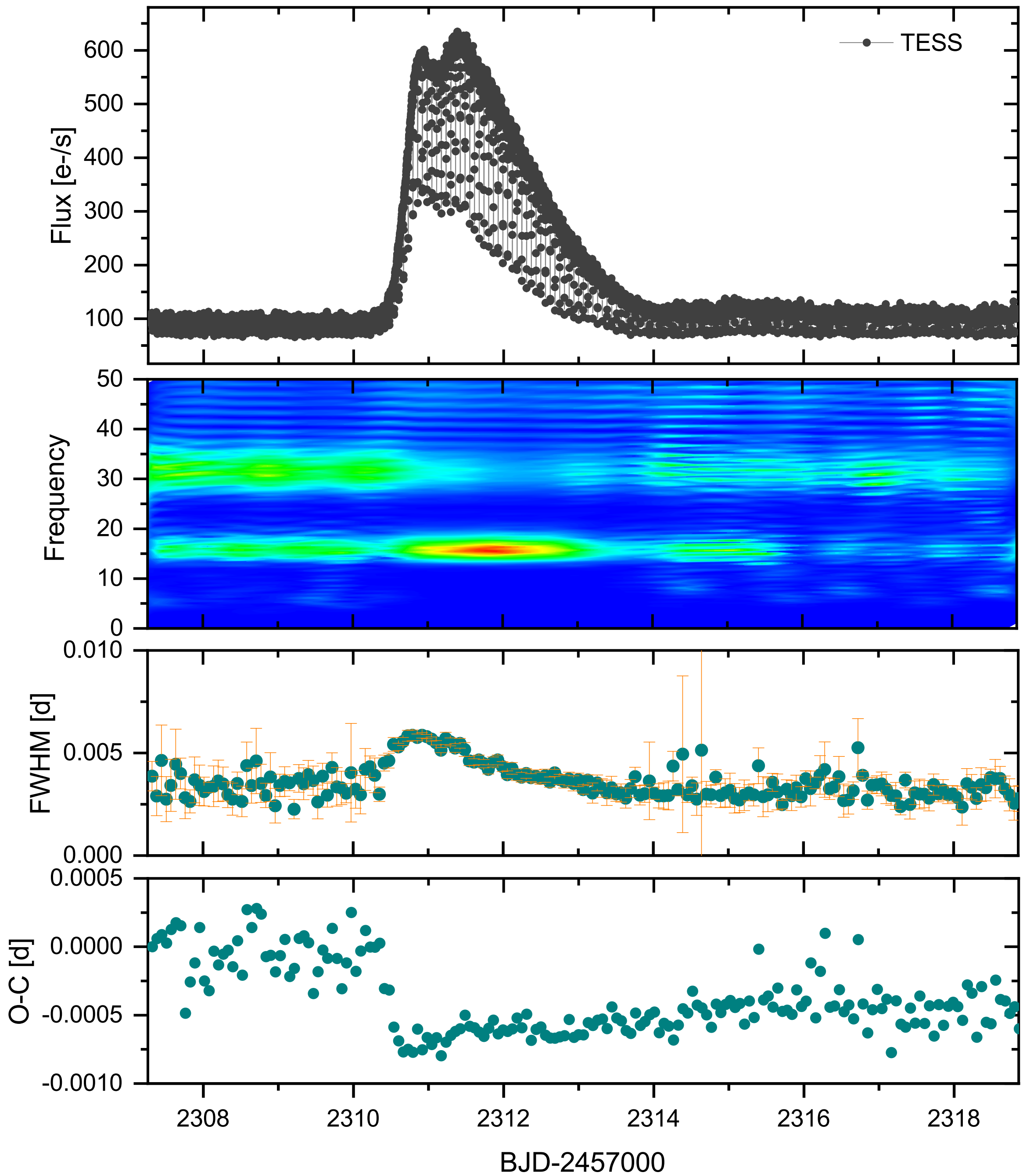

Fig. 6.— Top panel: the full TESS light curve of OY Car during outburst. From top to bottom, the remaining three panels show the weighted wavelet Z-transform around the orbital period's fundamental harmonic, the eclipse full width at half minimum, and the eclipse $O - C$ curve.

3.2.2. *Eclipse Depth Evolution*

Some recent studies revealed that, during quiescence, the eclipse depth is linearly related to the out-of-eclipse luminosity, and the slope of this correlation is nearly equal to one (e.g., Groot et al. 1998; Scaringi et al. 2013; Court et al. 2019, 2020; Han et al. 2021). As the outburst occurred, however, the eclipse depths show a departure from the expected relation and start to become less deep. As seen in Figure 3, the eclipse light curves of OY Car experience obvious variations in both its depth and shape during outburst. To trace changes in individual eclipse characteristics during an outburst, we perform a similar analysis using the data of these two outbursts of OY Car. Figure 7 shows the relation between the out-of-eclipse brightness and the eclipse depth for the superoutburst. We assessed the consistency of the predicted "line of maximal eclipse" with the quiescent data by applying a linear fit. In Figure 7, we utilized a linear model ($y = mx + n$) to analyze the quiescent data before the superoutburst began and acquired a slope $m = 0.56 \pm 0.05$ and an $x-$intercept $n = -152.9 \pm 18.7\ e^{-}s^{-1}$. This slope is markedly less than the unity gradient. While the "line of maximal eclipse" indicates the same part of the disk that is eclipsed during each orbital cycle. This indicates that the structure of the accretion disk during superoutbursts differs greatly from that of normal outbursts prior to the onset of the outburst. If we set the gradient back to 1 and refit the quiescent data, we determine an $x-$intercept of $-325.0 \pm 0.6\ e^{-}s^{-1}$. This varies greatly from the $x-$intercept that we obtain by using linear regression fitting. This implies that the structure of the accretion disk did change before the superoutburst.

In Figure 7, we also reveal the presence of hysteresis in eclipse depth-out of eclipse depth, indicating that the hysteresis found by Scaringi et al. (2013) during normal outbursts may also happen in superoutbursts. Moreover, we find that the rise branch before the appearance of the superhump is similar to the results of the previously reported targets (e.g., KIS J192748.53+444724.5, Scaringi et al. 2013; Z Cha, Court et al. 2019; IPHAS J051814.34+294113.2, Han et al. 2021). Since the superhump appeared, however, the hysteretic curve has evolved into a highly complex shape. This behavior appears to be connected to the more complex curve which is composed of eclipses, superhumps and precession of the elliptical disk.

In Figure 8, we show a plot of out-of-eclipse flux against eclipse depth for the normal outburst of OY Car. Again, a linear model is fitted to the quiescent data including the observations before and after the outburst. We find the slope $m = 0.87 \pm 0.02$, which is close to 1, though not precisely. Thus, we set $m = 1$ and refit the data to obtain an $x-$intercept of $-71.9 \pm 0.2\ e^{-}s^{-1}$. This value represents the flux emitted by the donor star when the entire disk is obscured.

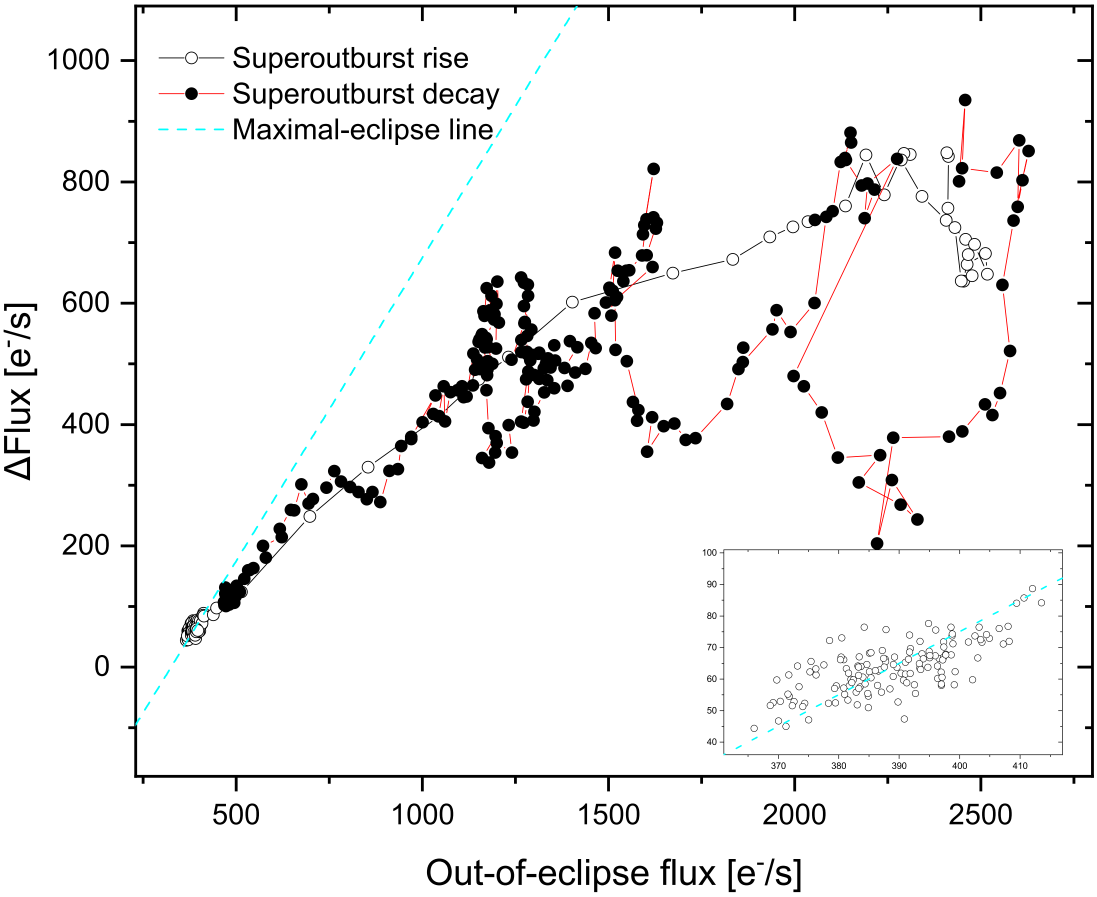

Fig. 7.— Relationship between the eclipse depth and the out-of-eclipse flux during superoutburst for all well-constrained eclipses in the TESS data of OY Car. The open solid circles denote the cycles during quiescence and outburst rise, the solide circles represents the outburst decline. The cyan dashed line represents the line of maximal eclipse by fitting a linear equation with the gradient=1 to the quiescent data. The inset shows a zoom to the eclipses used to calculate this line.

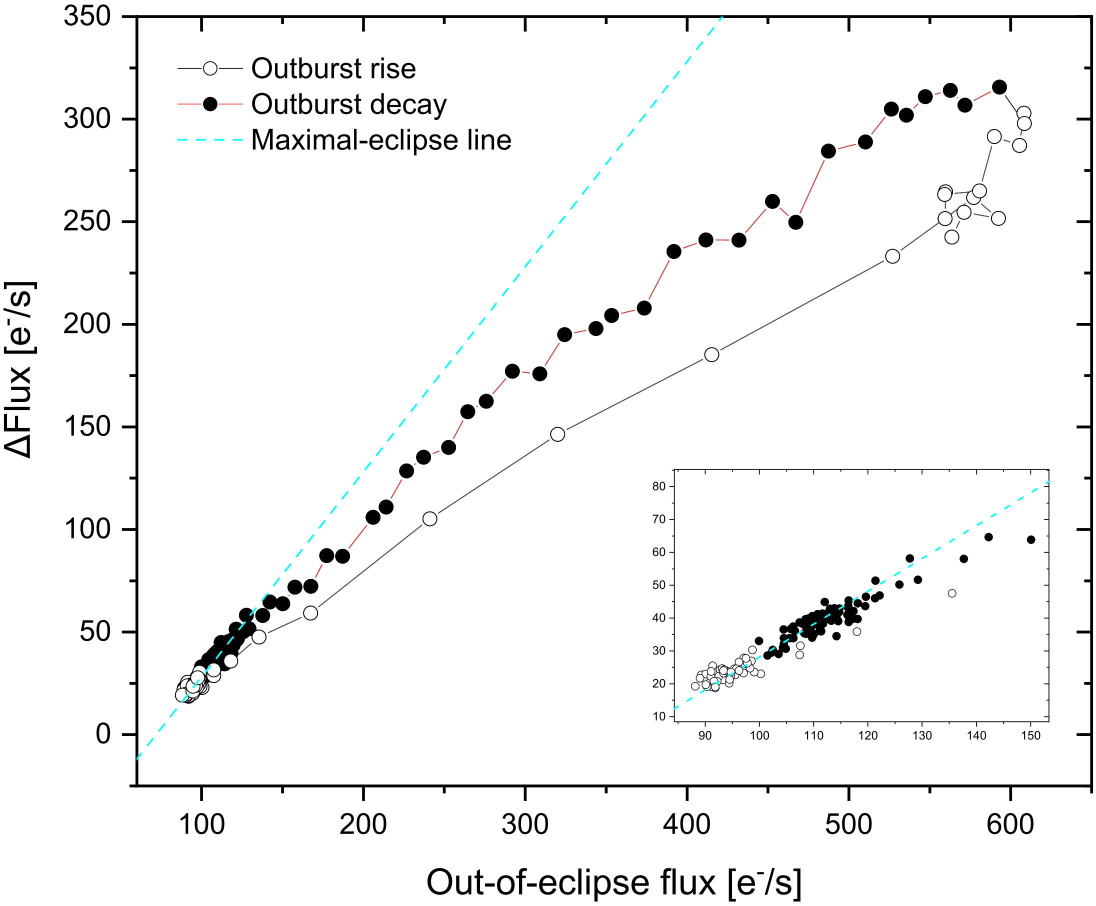

Fig. 8.— Relationship between the eclipse depth and the out-of-eclipse flux during normal outburst for all well-constrained eclipses in the TESS data of OY Car. The open solid circles denote the cycles during quiescence and outburst rise, the solide circles represents the outburst decline. The cyan dashed line represents the line of maximal eclipse by fitting a linear equation with the gradient=1 to the quiescent data. The inset shows a zoom to the eclipses used to calculate this line.

4. Discussion

4.1. Orbital Period Variations

4.1.1. Possible Interpretation of Long-term Period Increase

The upward parabolic variation in Figure 4 reveals a continuous increase at a rate of $+5.70 \times 10^{-13} s\, s^{-1}$. OY Car is a short-period CV below the period gap. The evolution of short-period CVs is driven by angular momentum losses (AMLs) associated with the emission of gravitational radiation (GR), resulting in its orbital period decrease (e.g., Knigge et al. 2011). Therefore, the observed period increase is not consistent with the secular decrease predicted by the CV evolutionary theory. One possibility is that this increase is caused by mass transfer from the less massive star onto the more massive. According to the evolution equation for the orbital period of the system (Robinson et al. 1991)

$$\frac{\dot{P}_{orb}}{P_{orb}} = \frac{3\zeta - 1}{2}\frac{\dot{M}_2}{M_2}, \tag{3}$$

the required mass transfer rate can be estimated. ζ is the mass-radius index and the orbital period increases for $\zeta < 1/3$. The orbital period of OY Car corresponds to a mass-radius index of $\zeta = 0.643$ in the revised model from Knigge et al. (2011). In this case, the required mass transfer rate to produce this increase is estimated to be $\dot{M}_2 \sim 10^{-9} M_{\odot} yr^{-1}$, which is at least three orders of magnitude higher than the published values in OY Car (e.g., Wood 1990; Pandel et al. 2005). Therefore, the mass transfer between white dwarf and donor star cannot be the reason for the long-term increase. The second possibility is that OY Car has evolved into a period bouncer and the donor has become a sub-stellar object. However, recent studies indicated that OY Car has a donor mass of $M_2 = 0.093 M_{\odot}$ above the hydrogen burning limit ($M_H = 0.063 M_{\odot}$ for CVs, McAllister et al. 2019) and is therefore not likely to be a period-bouncer. The most likely explanation for this change is that it is only a part of another longer and more complicated orbital period variation. More data are needed to check this possibility in the future.

4.1.2. Presence of a Third Body in OY Car?

Cyclic oscillations of the orbital period observed in CVs can be explained in general by the magnetic activity cycle in donors (i.e., Applegate mechanism, Applegate 1992), or the coupling of the spin of the active component with the orbital motion of the binary (so-called Applegate−Lanza mechanism, Lanza 2020), and the light travel-time effect via the presence of a potential third body. For OY Car, we first use the model refined by Brinkworth et al.

(2006) to calculate the energy requirement in the framework of Applegate mechanism. The result found that OY Car requires more than 50% of the available energy in a full cycle ($\Delta E/E_{sec} = 0.52$). During the analysis, we adopted the system parameters from McAllister et al. (2019) and the fitting parameters listed in Table 2. The donor luminosity can be calculated by $L_2 = (\frac{R_2}{R_\odot})^2(\frac{T_2}{T_\odot})^4 L_\odot$, in which $T_2 = 2805K$ for $M_2 = 0.093M_\odot$. A improved model from Völschow et al. (2016) has also been used to estimate the energy required to effect this change. The result, with the online calculator[3], shows that the minimum required energy divided by the available energy $\Delta E/E_{sec} = 0.45$. Overall, these results indicate that OY Car needs at least about half of the available energy to drive the Applegate mechanism. These authors also suggested that the low-mass systems with a donor mass of $0.30 - 0.36M_\odot$ are the most promising Applegate candidates (see Völschow et al. 2018). Ak et al. (2001) investigated the solar-type activity cycle of CV donors and found that the peak of the cycle periods is about 9.7 yr. Taken together, these results suggest that the best explanation for the cyclic modulation is probably not the magnetic activity.

We also try to assess whether the spin-orbit coupling model is the cause of this change. Combining the Lanza (2020) approximation for the relative amplitude of the variation of the angular velocity

$$\frac{\Delta\Omega}{\Omega} = -\frac{m{r_0}^2}{3I_s}\frac{\Delta P}{P}, \tag{4}$$

with the rotational energy change equation yields the relationship

$$\Delta E_{rot} = -[mr_0^2\Omega^2]\frac{\Delta t}{3T}, \tag{5}$$

where m is the reduced mass of the binary, $\Delta t/T = \Delta P/P$ is the amplitude of the period modulation, r_0 is the orbital radius of the active star and usually equal to its semi-major axis length. For OY Car, the relative amplitude $\Delta P/P \approx 3.27 \times 10^{-7}$, the reduced mass is $m = \frac{M_1 M_2}{M_1+M_2} = 0.084M_\odot$, and the angular velocity of the donor star is $\Omega = 2\pi/P_{orb} = 1.15 \times 10^{-3}s^{-1}$ due to the synchronous rotation of the system. Typically, the orbital radius corresponds to the secondary star's semimajor axis length ($r_0 = a_2 = 0.60R_\odot$). As a result, the rotational energy change of the active star is $\Delta E_{rot} \approx -6.75 \times 10^{33}J$ with a luminosity timescale of $\Delta E_{rot}/L_2 = 516.8$ yr, much longer than the modulation cycle. This means that even if the rotational energy dissipation during the operation of the mechanism is only 10%, the very feeble active star does not appear capable to supply the required energy along one cycle of the modulation. The results support the idea that the magnetic activity may not be the dominant mechanism in the case of OY Car.

[3]http://theory-starformation-group.cl/applegate/

More likely explanation would be the presence of a third body, leading to a light-travel-time effect on the eclipse light curves. We estimated the mass of the third body as $M_3 \sin i' = 0.011(\pm 0.003)M_\odot = 11.52(\pm 3.14)M_{Jup}$ based on the fitting results listed in Table 2 and the mass of two components of the binary. Considering the most likely scenario where the third body and the binary are coplanar, then its mass would match a giant planet in a circular orbit of a radius of 12.13(±0.36) au. However, the residuals in Figure 4 seem to show a lower-amplitude quasi-periodic modulation, implying that the magnetic activity still contribute to the orbital period variations. Consequently, the observed period variations in OY Car should be the result of the combined action of multiple mechanisms.

4.2. Outburst Properties of OY Car

4.2.1. Normal outburst

The normal outburst curve of OY Car is shown in Figure 6. Throughout the outburst, the depth, shape and FWHM value of the eclipses show distinct variations, indicating that the disk radius and the radial-temperature gradient variations. The mid-eclipse brightness during outburst is also constantly changing. Therefore, the disk is not entirely eclipsed by the donor star. To demonstrate this, we can perform the following calculation by comparing the donor star radius to the circularization radius of the disk, which can be obtained from (Frank et al. 2002)

$$\frac{R_{circ}}{a} = (1+q)(0.5 - 0.277 \log q)^4, \tag{6}$$

where a represents the orbital separation and q is the mass ratio. Applying the binary parameters from McAllister et al. (2019), we derived the smallest radius of the accretion disc $R_{circ} \sim 0.20R_\odot$. This value is significantly greater than the donor's radius of $\sim 0.14R_\odot$, implying that the accretion disk is always partially visible, even in quiescence. Our analysis yields a near 1 : 1 relationship between eclipse depth and the out-of-eclipse flux during the quiescent period before and after the normal outburst (the slope m=0.87). This relation corresponds to so-called "line of maximal eclipse", in which the same part of the disk be eclipsed during each cycle (Scaring et al. 2013). When we set the slope to 1, the intercept value of $-71.9\ e^- s^{-1}$ can be used as a rough estimate of the donor's flux. At the onset of the outburst, the data points rapidly deviate from the "line of maximal eclipse" and produce a clear hysteretic loop consists of rise and decay branches (see Figure 8). This implies the accretion disk expands during outburst to become larger than during quiescence.

The normal outburst of OY Car is a typical outside-in outburst (i.e., Type A), which has a rapid rise and a slower decay. The eclipse FWHM values are nearly maximal at the time of the outburst peak, supporting that the outburst initiated in the outer disk and propagated inward. An outburst originating in the outer disk leads to an immediate increase in eclipse width, as the donor star is unable to fully obscure the entire outbursting region. The rise time for the outside-in outburst can be calculated as (Frank et al. 2002)

$$t_r \sim \frac{R_d}{\alpha_h c_s}, \tag{7}$$

where R_d is the radius of the accretion disk, $\alpha_h c_s$ is the velocity of the inward-moving heating front. While the decay time is about ten times the rise time ($t_d \sim 10t_r$). During outbursts in dwarf novae, the outer disk radius is commonly approximated as $R_d \sim 0.9R_L$ (e.g., Smak 2001), where R_L is the effective radius of the primary star's Roche Lobe, which is calculated as $R_L \sim 0.21a$ for OY Car, using the given binary parameters and the approximate formulae developed by Eggleton (1983). The radius of accretion disk can be derived as $R_d \sim 0.9R_L \approx 0.88 \times 10^{10}$ cm. According to Frank et al. (2002), typical CV parameters during outbursts are $c_s \sim 2.5 \times 10^6$ cm/s and $\alpha_h \sim 0.1$. Using these parameters we derive $t_r \sim 9.78$ hr and $t_d \sim 4.08$ d, in rough agreement with observations 11.76 hr and 2.75 d.

The mid-eclipse times during outburst were observed to occur up to a few minutes earlier compared to quiescence (see $O - C$ curve in Figure 6). This timing shift is likely attributable to a reduced relative contribution from the hot spot to the system's total flux during the outburst. Since the hot spot is typically eclipsed after the central regions of the accretion disk, its diminished presence leads to an earlier observed eclipse minimum. In contrast, during quiescence, the hot spot contributes significantly to the light curve, resulting in a delayed eclipse minimum. During outburst, the disk's increased brightness compared to quiescence leads to its emission centroid being eclipsed earlier (Ramsay et al. 2017).

4.2.2. Superoutburst

In Figure 7, our analysis failed to produce a well-defined $1:1$ correlation to eclipse depth and out-of-eclipse flux prior to the superoutburst onset (the slope m=0.56). This implies that the quiescent disc's radius before the superoutburst was larger compared to the quiescent disc's radius during the periods surrounding normal outburst. The result supports the Tidal Thermal Instability (TTI) framework for superoutbursts (Osaki 1989), which suggests that each normal outburst removes less material from the disc compared to what has been added, causing a gradual increase in mass and size. To confirm such results, we checked AAVSO database, which contains the long-term light curves of the normal and superbursts referenced (see Figure 9). We then fit a function $f = a + b \times t$ to the non-outburst data to assess brightness changes before and after an outburst. The fitting parameters are summarized in Table 3, where we analyzed three data segments: prior to the superoutburst, following the superoutburst, and around the normal outburst. The results show that a rapid increase in flux prior to the superoutburst, with a rate of ~ 0.002 magnitudes per day. Following the superoutburst, the brightness declines sharply at a rate of ~ 0.006 magnitudes per day, indicating a faster decay than rise. Our analysis lends further support to previous prediction that the accretion disk radius reach a minimum following each superoutburst event (Osaki 1989). The overall fitting of the quiescent data around the normal outburst reveals a slow increase in brightness, with an increase rate of ~ 0.00015 magnitudes per day, supporting the key prediction of TTI model that the radius of the accretion disk during quiescence becomes slightly larger after each successive outburst. A superoutburst is triggered when the quiescent disk radius reaches a critical value, resulting in a reset to a smaller radius.

Around BJD 2458605.75, OY Car generated a precursor normal outburst, which subsequently triggered a superoutburst. Just after the precursor's peak, a decline in the eclipse FWHM and an increase in its depth were observed, precisely mirroring the behavior seen in another normal outburst (Figure 6). At BJD$\sim$2458607.97, the appearance of the first superhump marked the immediate rise of the light curve to superoutburst maximum. Following superoutburst peak, the superhump begins to fade, and its interaction with eclipses makes the light curve very complicated. The fade was observed to be centered on the coincidence of eclipse minima with superhump maxima. At this time, the eclipse FWHM begins to increase suddenly, until the superhump moves to a phase ~ 0.25 and then returns to the baseline (third panel in Figure 5). This indicates that the superhump fade is strongly dependent on the orbital phase. There are two possible explanations for this phenomenon. One is that a part of superhump light originates from the disk's vertically extended rim whose edge-on visibility varies across the orbital cycle (Osaki & Meyer 2003), An alternative hypothesis is the obscuration of the inner disk by vertically extended disk structure at specific orbital phases (Billington et al. 1996; Murray 1998).

During the superoutburst, the eclipse $O-C$ curve showed a clear quasi-periodic oscillation (Figure 5). During the period of dramatic eclipse FWHM variation, the eclipse $O-C$ timings also exhibited abrupt changes, implying that the origin of both changes should be the same. While the quasi-periodic variation provides strong evidence for the presence of an eccentric precessing disk in OY Car. In fact, previous authors have tried to find the eccentric disk in OY Car by the $O-C$ eclipse timings during the superoutburst (Krzeminski & Vogt 1985), but a later study by Naylor et al. (1987) indicated that the $O-C$ modulation showed reduced significance relative to earlier expectations due to a lack of data. Hessman et al. (1992) deduced the existence of an eccentric disk by analyzing variations in hot spot eclipse ingress times and the trajectory of the accretion stream. To obtain the precessional period of the disk, we fit a sine function to the quasi-periodic variation, and the best-fit model was displayed in the bottom panel of Figure 5 (magenta solid line). The best-fitting parameters parameters are listed in Table 4. The result reveals a precessional period of the disk as 2.84(±0.02) d, which is slightly longer than the period of 2.70 d presented by Krzeminski & Vogt (1985). The interaction between the precessional period and the orbital cycle would subsequently manifest as the superhump periodicity, which will be discussed in the next section.

Table 3: The best-fitting parameters of linear fits to quiescent data in Figure 9.

Linear Fitting: $f = a + b \times t$			
Parameters	Before "SO"	After "SO"	Surrounding "NO"
Weight	1.0	1.0	1.0
Intercept a	4874.41(±964.87)	11.32(±0.98)	15.66(±1.02)
Slope b	−0.00198(±0.00039)	+0.00623(±0.00146)	−0.00015(±0.00008)
Residual Sum of Squares	3.79	0.34	0.71

Table 4: Sinusoidal fit parameters to the $O - C$ diagram during superoutburst.

Sine Fitting: $(O-C)' = \Delta T_0{}' + K' \sin(\frac{\pi}{\omega} \times T' - \frac{\pi}{\omega} \times T'_C)$		
Parameters	Value	Error
$\Delta T_0{}'$	7.41×10^{-4}	2.09×10^{-5}
K'	4.62×10^{-4}	2.93×10^{-5}
ω	1.42	0.01
T'_C	−154.86	13.87
Residual sum of squares	8.85×10^{-8}	–
Reduced R-Square	0.55	–

4.3. Superhump Period and Evolution in OY Car

Previous studies reported several superhump periods in OY Car obtained from photometric data, they are: 0.064631 d (Krzeminski & Vogt 1985), 0.064245 d (Schoembs 1986) and 0.06454 d (Bruch et al. 1996). These periods are a few percent longer than the orbital period and are therefore positive superhumps. Based on the observed precessional period

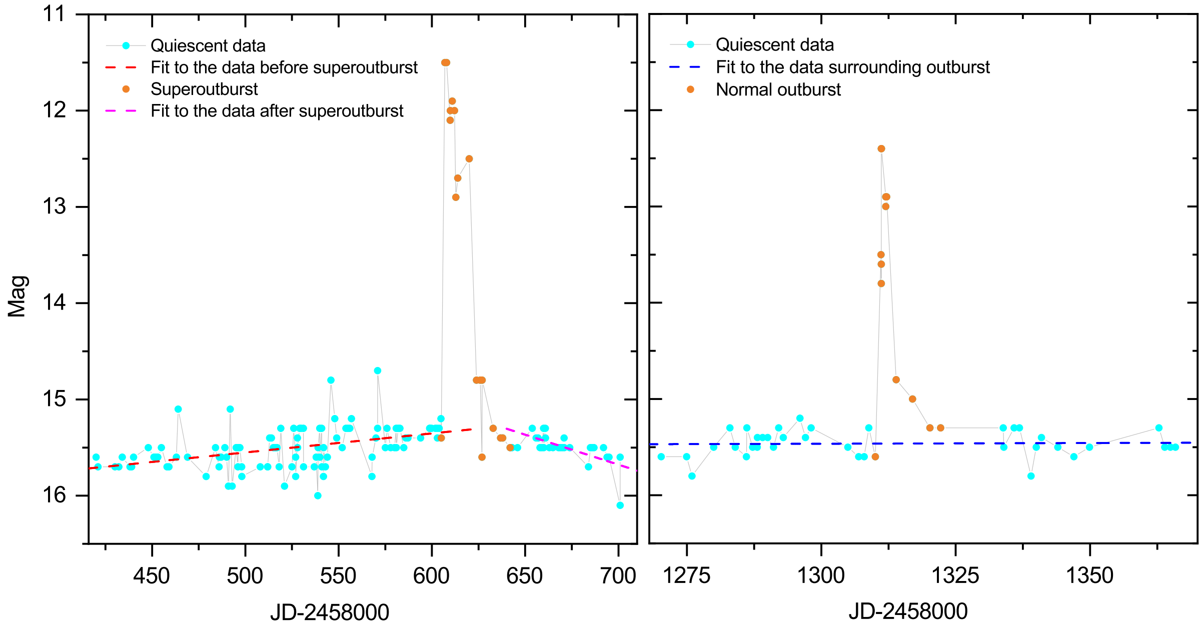

Fig. 9.— The AAVSO light curve corresponding to the same superoutburst and normal outburst of OY Car observed by TESS. Three dashed line are the linear fit to the quiescent data before, after superoutburst and surrounding normal outburst, respectively. The fitting parameters are listed in Table 3.

above and the orbital period, we can derive the superhump period by using the relation

$$\frac{1}{P_{sh}} = \frac{1}{P_{orb}} - \frac{1}{P_{prec}}, \quad (8)$$

where P_{sh} is the superhump period, and $P_{prec} = 2.84$ d is the precessional period. We obtained new superhump period $P_{sh} = 0.064556$ d, which is almost consistent with the previous results. The phenomenon of positive superhumps is attributed to the apsidal precession of an elliptical accretion disk, primarily driven by the 3:1 resonance (Whitehurst 1988; Hirose & Osaki 1990; Lubow 1991). This is an average superhump period that provides an independent method to determine the mass ratio q of the OY Car system components. The empirical relation between q and ϵ, as described by Knigge (2006), is employed:

$$q = (0.114 \pm 0.005) + (3.97 \pm 0.41) \times (\epsilon - 0.025), \quad (9)$$

where ϵ represents the superhump period excess, which can be determined by $\epsilon \equiv P_{sh}/P_{orb} - 1$. For OY Car, we obtain $\epsilon = 0.0227$ and $q = 0.1049(\pm 0.0051)$. The derived mass ratio is nearly consistent with previous estimates obtained by independent methods (e.g., McAllister et al. 2019).

In fact, the superhump period varies with time during superoutburst. To explore the superhump period drifts in OY Car, we conducted an $O - C$ analysis by fitting polynomials to the superhump maxima and determining their maximum times. The observed times of maxima were compared with those predicted by a linear ephemeris adopting our estimate of superhump period. The result is plotted in Figure 10 and shows three distinct stages A-B-C. The stage A is an initial growing stage with a longer superhump period; during the stage B, the superhump period increases smoothly over time, i.e., the period derivative $P_{dot} = \dot{P}/P$ is positive; the stage C shows a shorter, almost constant period. The positive P_{dot} for stage B superhumps has been reported in previous studies (Kato et al. 2015, 2017), but the limited observational coverage for individual superburst events suggests that the results remain inconclusive. Fortunately, TESS provides a complete and continuous superburst curve to obtain the full evolution of the superhumps (see Figure 10). A quadratic ephemeris was employed to model the $O-C$ diagram during the stage B. The result reveals the superhump period derivative $P_{dot} = +9.42 \times 10^{-5}$ days/cycle, which is almost consistent with the result given by Kato et al. (2015), confirming that a positive P_{dot} during stage B are reliable. The stage A superhumps are interpreted as corresponding to the dynamic precession rate at the radius of the 3:1 resonance with the system orbit (Osaki & Kato 2013). While the positive period derivatives during the stage B can be explained by the transient 2:1 resonance in the outer disk regulating the excitation and propagation of the 3:1 resonance (Kato et al. 2008). Stage C superhumps indicate a reactivation of the 3:1 resonance, occurring when superhumps in the outer disk are effectively suppressed (Kato et al. 2009). The evolution of superhumps in SU UMa-type dwarf novae, intrinsically linked to either the accretion disk radius or the propagation of an eccentricity wave, is expected to provide crucial diagnostics of the dynamics within outbursting accretion disks.

5. Conclusions

In this paper, a comprehensive photometric study of OY Car was carried out using ground-based data and TESS observations. The timing analysis reveals that this system undergoes an increase and a cyclic oscillation in the orbital period. The observed long-term increase is unlikely to result from mass transfer between two components or a period bouncer, and is instead interpreted as a segment of a longer and more complex period variations. Due to the insufficient energy of the donor star, the observed cyclic period variation cannot be explained by either the Applegate's mechanism or the Applegate-Lanza model (Lanza 2020). The cyclic variation is most plausibly explained by the gravitational influence of a potential celestial body orbiting the binary. The mass of the tertiary object was determined to be $M_3 \sin i^{'} = 11.52(\pm 3.14) M_{Jup}$. Assuming coplanarity between the third body and the eclipsing binary, the mass would correspond to that of a giant planet in a circular orbit. The residuals in Figure 4 appear to exhibit a low-amplitude quasi-periodic modulation, revealing that the orbital period variation of OY Car is quite complex. While several planetary candidates have been reported around CVs (e.g., Qian et al. 2015; Court et al. 2019; Han et al. 2017, 2023), they have not yet been independently confirmed by other observational methods. Astrometry holds strong potential for future confirmation of these candidates via detection of their transverse motion (Marsh 2018).

The TESS light curve contains one superoutburst lasting $\sim$ 18 d and one normal, outside-in outburst lasting $\sim$ 4 d. We analyze the changes in eclipse depth and out-of-eclipse flux throughout both outburst and superoutburst events. We find that the eclipse depth and out-of-eclipse light levels exhibit a linear correlation during quiescence. Linear fits to quiescent data reveal near-unity slopes before normal outbursts but significantly lower values before superoutbursts, indicating distinct structural changes in the accretion disk prior to superoutbursts. This is consistent with the thermal-tidal instability (TTI) model and supported by long-term AAVSO light curve analysis. With the onset of outburst, however, this relationship departed from linearity, producing clear hysteresis loops. The hysteretic shape during normal outburst implies that the disk expands during outburst to become larger than the donor star. As for the superoutburst, the hysteretic shape is very complex and difficult to interpret. We also performed an eclipse analysis during the outbursts which reveals that the normal outburst is an outside-in outburst and shows a systematic change

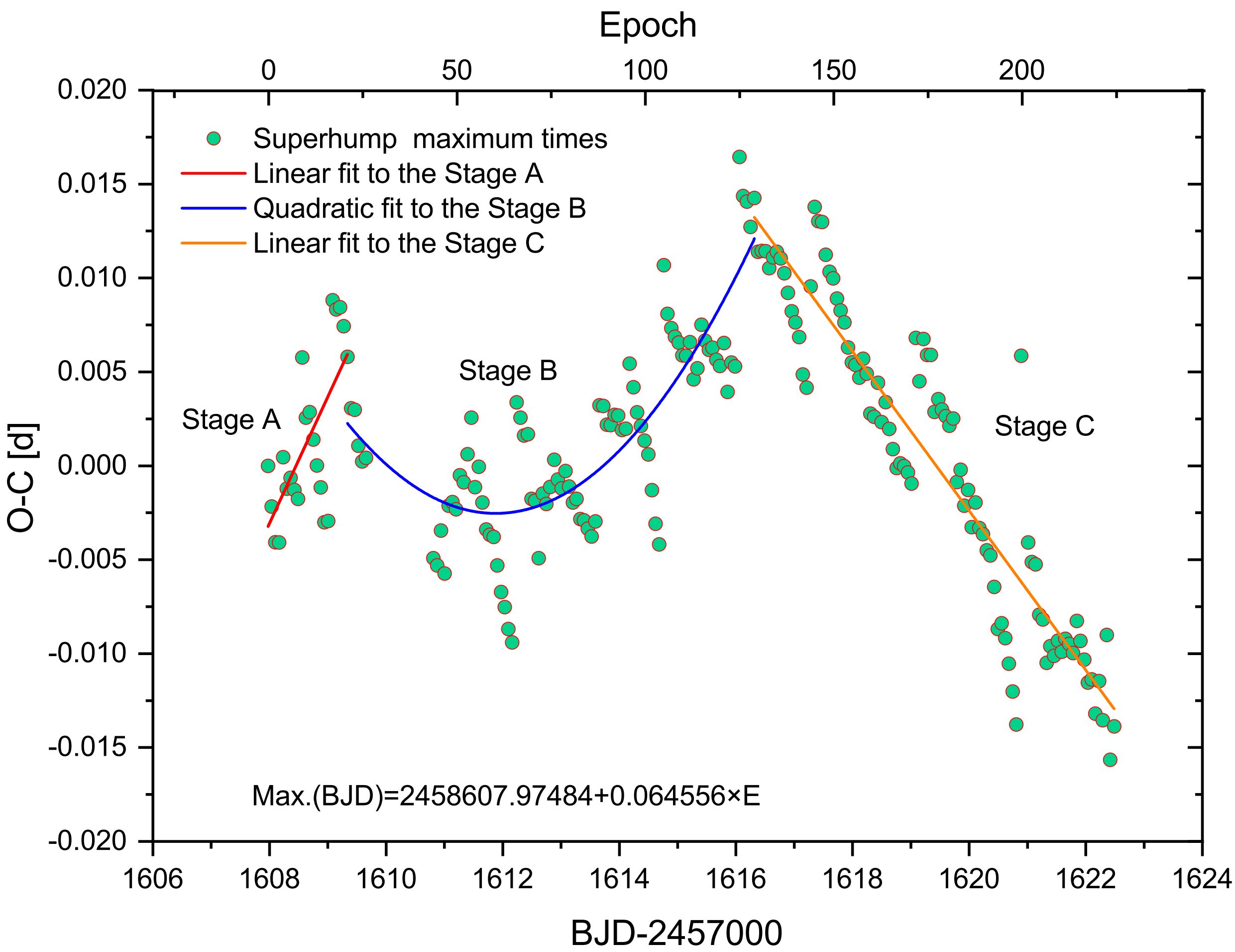

Fig. 10.— The $O-C$ diagram of superhump maximum times, showing three distinct stages (A-B-C). The red and orange solid lines are the linear fit to the data in the stage A and C, respectively. The blue solid line is a quadratic ephemeris fit to the superhumps in the stage B. The upward parabola reveals that superhump period derivative is positive during this stage.

in the hot spots contribution to the total luminosity. During superoutburst, the $O - C$ diagram shows a quasi-periodic modulation, indicating the presence of an eccentric, precessing accretion disk in OY Car, with a precession period of 2.84 d.

We also study the properties of the superhumps. The superhump period is determined to be $P_{sh} = 0.064556$ d by using the beat relation, identifying it as a positive superhump. Then the mass ratio of OY Car is estimated to be $q = 0.1049(\pm 0.0051)$ from the superhump period excess, which is in close agreement with previous estimates obtained through independent methods. To investigate the superhump evolution in OY Car, we performed an $O-C$ analysis of the superhump maxima. The results reveal three distinct stages (A-B-C), characterized by a longer initial period in stage A, a smoothly increasing period during stage B with $P_{dot} = +9.42 \times 10^{-5}$, and a nearly constant, shorter period in stage C. These findings, supported by uninterrupted TESS coverage, confirm the reliability of a positive P_{dot} in stage B, consistent with previous studies. The superhump period evolution likely reflects changes in the accretion disk structure and resonance dynamics, with future high-cadence space-based data expected to further constrain the underlying physical mechanisms.

This work is partly supported by the Yunnan Fundamental Research Projects (Grant Nos. 202301AT070299, 202401CF070039) and the Yunnan Students' Innovative Entrepreneurship Training Program (No. 202411390003). The authors gratefully acknowledge the computing support provided by the JRT Science Data Center at Yuxi Normal University. The new photometric observations presented here were made with the 2.15-m Jorge Sahade telescope in Argentina. Moreover, this paper includes data collected by the TESS mission, downloaded from the Mikulski Archivefor Space Telescopes (MAST). Funding for the TESS mission is provided by the NASA Explorer Program. We also appreciate the contributions of the AAVSO database and the International Variable Star Index database (VSX[4]) in this research.

REFERENCES

Ak, T., Ozkan, M. T., & Mattei, J. A. 2001, A&A, 369, 882. doi:10.1051/0004-6361:20010167

Applegate, J. H. 1992, ApJ, 385, 621. doi:10.1086/170967

Baptista, R. 2016, Astronomy at High Angular Resolution, 439, 155. doi:10.1007/978-3-319-39739-9_9

[4]https://vsx.aavso.org/

Baskill, D. S., Wheatley, P. J., & Osborne, J. P. 2005, MNRAS, 357, 2, 626. doi:10.1111/j.1365-2966.2005.08677.x

Billington, I., Marsh, T. R., Horne, K., et al. 1996, MNRAS, 279, 4, 1274. doi:10.1093/mnras/279.4.1274

Bonnet-Bidaud, J. M., Motch, C., & Mouchet, M. 1985, A&A, 143, 313.

Brinkworth, C. S., Marsh, T. R., Dhillon, V. S., et al. 2006, MNRAS, 365, 1, 287. doi:10.1111/j.1365-2966.2005.09718.x

Bruch, A., Beele, D., & Baptista, R. 1996, A&A, 306, 151.

Collins, K. A., Collins, K. I., Pepper, J., et al. 2018, AJ, 156, 5, 234. doi:10.3847/1538-3881/aae582

Cook, M. C. 1985, MNRAS, 215, 211. doi:10.1093/mnras/215.2.211

Copperwheat, C. M., Marsh, T. R., Parsons, S. G., et al. 2012, MNRAS, 421, 1, 149. doi:10.1111/j.1365-2966.2011.20282.x

Court, J. M. C., Scaringi, S., Rappaport, S., et al. 2019, MNRAS, 488, 3, 4149. doi:10.1093/mnras/stz2015

Court, J. M. C., Scaringi, S., Littlefield, C., et al. 2020, MNRAS, 494, 4, 4656. doi:10.1093/mnras/staa1042

Eggleton, P. P. 1983, ApJ, 268, 368. doi:10.1086/160960

Frank, J., King, A., & Raine, D. J. 2002, Accretion Power in Astrophysics (Cambridge: Cambridge Univ. Press), 54

Greenhill, J. G., Hill, K. M., Dieters, S., et al. 2006, MNRAS, 372, 3, 1129. doi:10.1111/j.1365-2966.2006.10920.x

Groot, P. J., Augusteijn, T., Barziv, O., et al. 1998, A&A, 340, L31. doi:10.48550/arXiv.astro-ph/9810357

Han, Z.-T., Qian, S.-B., Fernández Lajús, E., et al. 2015, New A, 34, 1. doi:10.1016/j.newast.2014.04.011

Han, Z.-T., Qian, S.-B., Irina, V., et al. 2017, AJ, 153, 5, 238. doi:10.3847/1538-3881/aa6c2a

Han, Z.-T., Soonthornthum, B., Qian, S.-B., et al. 2021, AJ, 162, 5, 205. doi:10.3847/1538-3881/ac250b

Han, Z.-T., Qian, S.-B., Han, Q.-W., et al. 2023, ApJ, 953, 1, 63. doi:10.3847/1538-4357/acdd6e

Hartman, J. D. & Bakos, G. Á. 2016, Astronomy and Computing, 17, 1. doi:10.1016/j.ascom.2016.05.006

Harvey, D., Skillman, D. R., Patterson, J., et al. 1995, PASP, 107, 551. doi:10.1086/133591

Hessman, F. V., Mantel, K.-H., Barwig, H., et al. 1992, A&A, 263, 147.

Hirose, M. & Osaki, Y. 1990, PASJ, 42, 135.

Horne, K. 1985, MNRAS, 213, 129. doi:10.1093/mnras/213.2.129

Kato, T., Maehara, H., & Monard, B. 2008, PASJ, 60, L23. doi:10.1093/pasj/60.4.L23

Kato, T., Imada, A., Uemura, M., et al. 2009, PASJ, 61, S395. doi:10.1093/pasj/61.sp2.S395

Kato, T., Hambsch, F.-J., Dubovsky, P. A., et al. 2015, PASJ, 67, 6, 105. doi:10.1093/pasj/psv072

Kato, T., Isogai, K., Hambsch, F.-J., et al. 2017, PASJ, 69, 5, 75. doi:10.1093/pasj/psx058

Kimura, M. & Osaki, Y. 2021, PASJ, 73, 5, 1225. doi:10.1093/pasj/psab069

Knigge, C. 2006, MNRAS, 373, 2, 484. doi:10.1111/j.1365-2966.2006.11096.x

Knigge, C., Baraffe, I., & Patterson, J. 2011, ApJS, 194, 2, 28. doi:10.1088/0067-0049/194/2/28

Krzeminski, W. & Vogt, N. 1985, A&A, 144, 124.

Lanza, A. F. 2020, MNRAS, 491, 2, 1820. doi:10.1093/mnras/stz3135

Lasota, J.-P. 2001, New A Rev., 45, 7, 449. doi:10.1016/S1387-6473(01)00112-9

Lubow, S. H. 1991, ApJ, 381, 268. doi:10.1086/170648

Mauche, C. W. 1998, Wild Stars in the Old West, 137, 113. doi:10.48550/arXiv.astro-ph/9709101

Mauche, C. W. & Raymond, J. C. 2000, ApJ, 541, 2, 924. doi:10.1086/309489

McAllister, M., Littlefair, S. P., Parsons, S. G., et al. 2019, MNRAS, 486, 4, 5535. doi:10.1093/mnras/stz976

Montgomery, M. M. 2009, MNRAS, 394, 4, 1897. doi:10.1111/j.1365-2966.2009.14487.x

Motch, C. 1981, A&A, 100, 277.

Murray, J. R. 1998, MNRAS, 297, 1, 323. doi:10.1046/j.1365-8711.1998.01504.x

Naylor, T., Charles, P. A., Hassall, B. J. M., et al. 1987, MNRAS, 229, 183. doi:10.1093/mnras/229.2.183

Osaki, Y. 1989, PASJ, 41, 1005.

Osaki, Y. 1996, PASP, 108, 39. doi:10.1086/133689

Osaki, Y. & Meyer, F. 2003, A&A, 401, 325. doi:10.1051/0004-6361:20030115

Osaki, Y. & Kato, T. 2013a, PASJ, 65, 50. doi:10.1093/pasj/65.3.50

Osaki, Y. & Kato, T. 2013b, PASJ, 65, 95. doi:10.1093/pasj/65.5.95

Pandel, D., Córdova, F. A., Mason, K. O., et al. 2005, ApJ, 626, 1, 396. doi:10.1086/429983

Patterson, J. 1999, Disk Instabilities in Close Binary Systems, 26, 61.

Pilarčík, L., Wolf, M., Zasche, P., et al. 2018, New A, 60, 1. doi:10.1016/j.newast.2017.09.005

Pratt, G. W., Hassall, B. J. M., Naylor, T., et al. 1999, MNRAS, 309, 4, 847. doi:10.1046/j.1365-8711.1999.02900.x

Press, W. H., Teukolsky, S. A., Vetterling, W. T., et al. 1992, Numerical recipes in FORTRAN. The art of scientific computing (2nd ed.; Cambridge: Cambridge Univ. Press)

Qian, S. B., Han, Z. T., Fernández Lajús, E., et al. 2015, ApJS, 221, 1, 17. doi:10.1088/0067-0049/221/1/17

Ramsay, G., Poole, T., Mason, K., et al. 2001a, A&A, 365, L288. doi:10.1051/0004-6361:20000039

Ramsay, G., Córdova, F., Cottam, J., et al. 2001b, A&A, 365, L294. doi:10.1051/0004-6361:20000042

Ramsay, G., Wood, M. A., Cannizzo, J. K., et al. 2017, MNRAS, 469, 1, 950. doi:10.1093/mnras/stx859

Ricker, G. R., Winn, J. N., Vanderspek, R., et al. 2014, Proc. SPIE, 9143, 914320. doi:10.1117/12.2063489

Ricker, G. R., Winn, J. N., Vanderspek, R., et al. 2015, Journal of Astronomical Telescopes, Instruments, and Systems, 1, 014003. doi:10.1117/1.JATIS.1.1.014003

Ricker, G. R., Vanderspek, R., Winn, J., et al. 2016, Proc. SPIE, 9904, 99042B. doi:10.1117/12.2232071

Robinson, E. L., Shetrone, M. D., & Africano, J. L. 1991, AJ, 102, 1176. doi:10.1086/115944

Scaringi, S., Groot, P. J., & Still, M. 2013, MNRAS, 435, L68. doi:10.1093/mnrasl/slt099

Schoembs, R. 1986, A&A, 158, 233.

Smak, J. I. 2001, Acta Astron., 51, 295.

Smak, J. 2013, Acta Astron., 63, 3, 369. doi:10.48550/arXiv.1307.1228

Tody, D. 1986, Proc. SPIE, 627, 733. doi:10.1117/12.968154

Tody, D. 1993, Astronomical Data Analysis Software and Systems II, 52, 173.

Vogt, N. 1974, A&A, 36, 369.

Vogt, N., Schoembs, R., Krzeminski, W., et al. 1981, A&A, 94, L29.

Vogt, N. 1982, ApJ, 252, 653. doi:10.1086/159592

Völschow, M., Schleicher, D. R. G., Perdelwitz, V., et al. 2016, A&A, 587, A34. doi:10.1051/0004-6361/201527333

Völschow, M., Schleicher, D. R. G., Banerjee, R., et al. 2018, A&A, 620, A42. doi:10.1051/0004-6361/201833506

Warner, B. 2003, , 592. doi:10.1017/CBO9780511586491

Whitehurst, R. 1988, MNRAS, 232, 35. doi:10.1093/mnras/232.1.35

Whitehurst, R. & King, A. 1991, MNRAS, 249, 25. doi:10.1093/mnras/249.1.25

Wood, J. H., Horne, K., Berriman, G., et al. 1989, ApJ, 341, 974. doi:10.1086/167557

Wood, J. H., Irwin, M. J., & Pringle, J. E. 1985, MNRAS, 214, 475. doi:10.1093/mnras/214.4.475

Wood, J. H. 1990, MNRAS, 243, 219.

Wood, M. A., Thomas, D. M., & Simpson, J. C. 2009, MNRAS, 398, 4, 2110. doi:10.1111/j.1365-2966.2009.15252.x

Wood, M. A., Still, M. D., Howell, S. B., et al. 2011, ApJ, 741, 2, 105. doi:10.1088/0004-637X/741/2/105

Woudt, P. A. & Warner, B. 2009, MNRAS, 400, 2, 835. doi:10.1111/j.1365-2966.2009.15488.x

This preprint was prepared with the AAS LaTeX macros v5.2.